ELSEVIER

Engineering Analysis with Boundary Elements 30 (2006) 910–924

ENGINEERING ANALYSIS with BOUNDARY ELEMENTS

www.elsevier.com/locate/enganabound

Modeling of the ground plane in electrostatic BEM analysis of MEMS and NEMS

Hui Chen, Subrata Mukherjee*

Department of Theoretical and Applied Mechanics, Kimball Hall, Cornell University, Ithaca, NY 14853, USA

Received 7 December 2005; accepted 7 March 2006
Available online 11 September 2006

Abstract

This paper is concerned with calculation of charge distribution on conducting elements in microelectromechanical and nanoelectromechanical systems (MEMS and NEMS). The conductors are beam like in MEMS or nanotubes in NEMS. The ground plane is typically present in such problems. This is usually modeled by constructing image elements with the ground treated as a flat mirror, thereby doubling the size of a problem. An alternative approach is to model the ground directly in a boundary element method (BEM) formulation of the problem. The latter approach is adopted in this paper. The governing BEM equations, and their regularization, is discussed in detail. Numerical results are presented for selected examples and their results are compared with analytical solutions whenever possible.

Keywords: Boundary element methods; Microelectromechanical systems; Nanoelectromechanical systems; Beams; Nanotubes; Modeling of ground

1. Introduction

Microelectromechanical systems (MEMS) have demonstrated important applications in a wide variety of industries including mechanical and aerospace, medicine, communications, information technology etc. Nanoelectromechanical systems (NEMS) are "smaller" MEMS in the sense that they have submicron critical dimensions. Owing primarily to their small size, NEMS can offer very high sensitivities (e.g. force sensitivities at the attonewton level, mass sensitivities at a single molecule or even a single atom level, and charge sensitivities at the level of the charge on a single electron). In addition, they offer mechanical quality factors in the tens of thousands and fundamental frequencies in the microwave range [1,2]. Fabrication of silicon nanotweezers [3] and nanoresonators [4] has been demonstrated recently. Carbon nanotubes (CNTs) have remarkable properties—they are very stiff, have low density, ultra-small cross-sections and can be defect free. They offer fascinating applications possibilities. Natural frequencies of tunable CNTs have been measured recently [5].

Numerical simulation of electrically actuated MEMS devices have been carried out for around a decade or so by using the boundary element method (BEM—see, e.g. [6–10]) to model the exterior electric field and the finite element method (FEM—see, e.g. [11–13]) to model deformation of the structure. The commercial software package MEMCAD [14], for example, uses the commercial FEM software package ABAQUS for mechanical analysis, together with a BEM code FastCap [15] for the electric field analysis. Other examples of such work are [16–19]; as well as [14,20,21] for dynamic analysis of MEMS. A very nice recent example of NEMS simulation is [22]. This paper employs the classical electrostatic model for nano conductors and three different electrostatic models: classical, semiclassical and quantum-mechanical, for semiconductors.

Many applications in MEMS and NEMS require BEM analysis of the electric field exterior to thin conducting objects. In the context of MEMS with very thin beams or plates (see Fig. 1), a convenient way to model such a problem is to assume plates (or beams) with vanishing

*Corresponding author. Tel.: +1 607 255 7143; fax: +1 607 255 2011.
E-mail address: sm85@cornell.edu (S. Mukherjee).

0955-7997/$ - see front matter © 2006 Elsevier Ltd. All rights reserved.
doi:10.1016/j.enganabound.2006.03.013

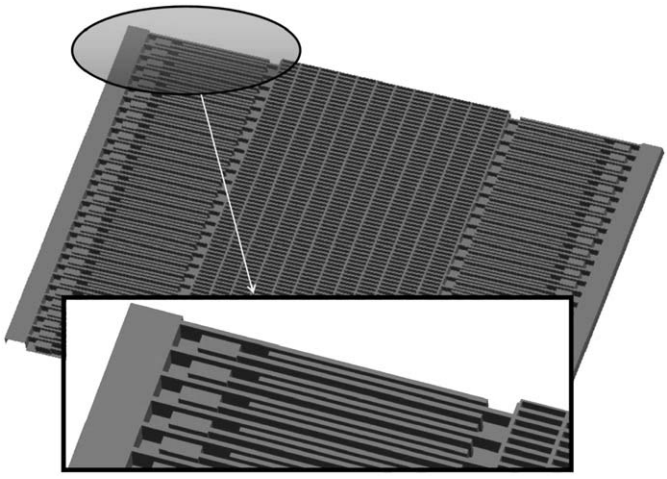

Fig. 1. Parallel plate resonator: geometry and detail of the parallel plate fingers (from [23]).

thickness and solve for the sum of the charges on the upper and lower surfaces of each plate [24] (or beam). The standard boundary integral equation (BIE) with a weakly singular kernel is used in [24] and this approach works well for determining, for example, the capacitance of a parallel plate capacitor. For MEMS calculations, however, one must obtain the charge densities separately on the upper and lower surfaces of a plate (or beam) since the traction at a surface point on a plate (or beam) depends on the square of the charge density at that point. The gradient BIE is employed in [25] to obtain these charge densities separately. The formulation given in [25] is a BEM scheme that is particularly well-suited for MEMS analysis of very thin plates—for $h/L \leqslant 0.001$—in terms of the length L (of a side of a square plate) and its thickness h. A similar approach has also been developed for MEMS with very thin beams [26]. Similar work has also been reported recently by Chuyan et al. [27] in the context of determining fringing fields and levitating forces for 2D beam shaped conductors in MEMS combdrives. A fully coupled BEM/FEM MEMS calculation with very thin plates has just been completed [28]. See, also, [29] for an application of the thin plate idea for modeling damping forces on MEMS with thin plates.

Another interesting problem that has been solved recently deals with charge distribution on thin conducting CNTs [30]. A line model for a nanotube is proposed here. As before for beams and plates, this model overcomes the problem of dealing with nearly singular matrices that occur when the standard BEM is applied to very thin features (objects or gaps). The charge distribution per unit length on the surface of a nanotube is obtained first. The charge density per unit area on the entire nanotube surface is obtained next by a post-processing step. This new approach is very efficient. Numerical results are presented for various examples. Results for selected problems are compared with those from a full 3D BEM calculation [31] as well as with available analytical solutions [32]. Excellent agreement is obtained with available analytical solutions.

In MEMS and NEMS calculations of the type considered here, ground planes are typically present. The typical approach for dealing with this issue is to construct an image plane with the ground plane treated as a flat mirror. This, of course, doubles the size of a given problem. The BEM formulation is modified in the present work so that the ground plane is modeled directly. Problems with conducting beams are considered first. This is followed by problems with thin conducting nanotubes.

An alternative way of modeling the ground plane is to use half-space Green's functions in the BEM formulation. This approach is presented in [30] for nanotube problems. One advantage of the approach discussed in the present paper is that, unlike in other formulations, the charge distribution on the ground is also obtained here. This information can be useful in certain problems.

The present paper is organized as follows BIEs are first presented for an infinite region containing two thin conducting beams. This is followed by BIEs in a semi-infinite region containing one thin conducting beam and the ground. The next section deals with a semi-infinite region containing an arbitrary number of beams, together with the ground plane. Each beam can be of arbitrary length and be oriented in an arbitrary direction, but their mid-planes must all lie in the same plane. Numerical results are presented for some beam problems. Analysis of conducting nanotubes follows using the same format as described above. A concluding remarks section completes the paper.

2. BIEs in infinite region containing two thin conducting beams

Consider the situation shown in Fig. 2 with two parallel beams. Of interest is the solution of the following Dirichlet problem for Laplace's equation:

$$\nabla^2\phi(\mathbf{x}) = 0, \quad \mathbf{x} \in B, \quad \phi(\mathbf{x}) \quad \text{prescribed for } \mathbf{x} \in \partial B, \qquad (1)$$

where ϕ is the potential and B is the region *exterior* to the two beams, each of length L and height h. The unit normal $\mathbf{n}$ to ∂B is defined to point away from B (i.e. into a beam).

2.1. Regular BIE—source point approaching a beam surface s_1^+

It is first noted that, for this problem, one can write (see, e.g. [26,33]):

$$\phi(\boldsymbol{\xi}) = -\int_s \frac{\ln r(\boldsymbol{\xi}, \mathbf{y})\sigma(\mathbf{y})\, \mathrm{d}s(\mathbf{y})}{2\pi\varepsilon} + C, \qquad (2)$$

where σ is the charge density, per unit area, at a point on a beam surface and s is the total surface of the two beams. Also, $\mathbf{r}(\boldsymbol{\xi}, \mathbf{y}) = \mathbf{y} - \boldsymbol{\xi}$ (with $\boldsymbol{\xi}$ a source and $\mathbf{y}$ a field point), $r = |\mathbf{r}|$, and ε is the dielectric constant of the medium outside the conductors. The constant C is given by the

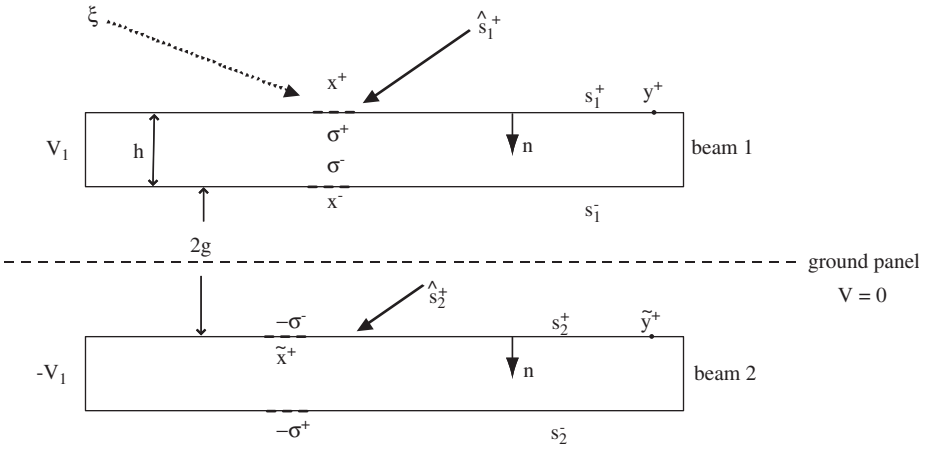

Fig. 2. Two parallel conducting beams.

expression [33]:

$$C = \phi_\infty - G(R_\infty)Q, \tag{3}$$

where ϕ_∞ and $G(R_\infty)$ are the potential and the Green's function at infinity, respectively, and Q is the total charge (per unit beam width) on the two beams. In the above, the Green's function is $G(\mathbf{x},\mathbf{y}) = -\ln r(\mathbf{x},\mathbf{y})/(2\pi\varepsilon)$. Also, one has $Q_\infty = -Q$, where Q_∞ is the total charge at infinity. For the problem under consideration, $Q = 0$, so that $C = \phi_\infty$.

Next, Eq. (2) is written for the special case of very thin beams (i.e. $h/L \ll 1$). One now gets:

$$\phi(\boldsymbol{\xi}) = -\int_{s_1^+ \cup s_2^+} \frac{\ln r(\boldsymbol{\xi},\mathbf{y}) q(\mathbf{y})}{2\pi\varepsilon}\, \mathrm{d}s(\mathbf{y}) + C, \tag{4}$$

where $q(\mathbf{y}) = \sigma(\mathbf{y}^+) + \sigma(\mathbf{y}^-)$.

As $\boldsymbol{\xi} \to \mathbf{x}^+ \in \hat{s_1}^+ \subset s_1^+$ (see Fig. 2—here $\hat{s_1}^+$ is a neighborhood of $\mathbf{x}^+$), one can write Eq. (4) as

$$\phi(\mathbf{x}^+) = -\int_{s_1^+ \cup s_2^+} \frac{\ln r(\mathbf{x}^+,\mathbf{y}) q(\mathbf{y})}{2\pi\varepsilon}\, \mathrm{d}s(\mathbf{y}) + C \tag{5}$$

and then as

$$\begin{aligned}\phi(\mathbf{x}^+) = & -\int_{s_1^+ - \hat{s_1}^+} \frac{\ln r(\mathbf{x}^+,\mathbf{y}) q(\mathbf{y})}{2\pi\varepsilon}\, \mathrm{d}s(\mathbf{y}) \\ & -\int_{\hat{s_1}^+} \frac{\ln r(\mathbf{x}^+,\mathbf{y}) q(\mathbf{y})}{2\pi\varepsilon}\, \mathrm{d}s(\mathbf{y}) \\ & -\int_{s_2^+} \frac{\ln r(\mathbf{x}^+,\mathbf{y}) q(\mathbf{y})}{2\pi\varepsilon}\, \mathrm{d}s(\mathbf{y}) + C.\end{aligned} \tag{6}$$

The constant C in (6) is unknown and a constraint equation is needed to determine this constant. This equation is

$$\int_{s_1^+ \cup s_2^+} q(\mathbf{y})\, \mathrm{d}s(\mathbf{y}) = Q = 0. \tag{7}$$

The second integral on the right-hand side of (6) is logarithmically singular, while the rest are usually regular. It should be noted, however, that the last integral on the right-hand side of (6) becomes nearly logarithmically singular when the gap $2g$ between the beams is very small. Numerical evaluation of nearly logarithmically singular integrals is discussed, for example, in [26]. It should be mentioned, however, that the thin feature BEM approach presented in this paper breaks down if $2g \approx h$ (see Fig. 2). In other words, the gap $2g$ can be very small but must be at least around $3h$ for this method to work [28].

A similar equation can be written for $\tilde{\mathbf{x}}^+ \in s_2^+$. For the case shown in Fig. 2 (with $\phi_1 = V_1$, $\phi_2 = -V_1$), however, this is not necessary since $q(\mathbf{y})$ is equal and opposite on the two beams. Also, for this case, $\phi_\infty = C = 0$ [26]. Therefore, Eq. (6) is sufficient to solve for q on both the beams!

2.2. Gradient BIE—source point approaching a beam surface s_1^+

It is first noted that for $\mathbf{x} \in s_k^+ \cup s_k^-$, $k = 1, 2$:

$$\sigma(\mathbf{x}) = \varepsilon \frac{\partial \phi}{\partial n}(\mathbf{x}) = \varepsilon \mathbf{n}(\mathbf{x}) \cdot [\nabla_\xi \phi(\boldsymbol{\xi})]_{\boldsymbol{\xi}=\mathbf{x}}. \tag{8}$$

Consider the limit $\boldsymbol{\xi} \to \mathbf{x}^+ \in s_1^+$. (It is important to realize that this limit is meaningless for a point $\mathbf{x}$ on either end of a beam since the charge density is singular at these locations). One has

$$\sigma(\mathbf{x}^+) = \oint\!\!\!\!\!\!= \int_{s_1^+ \cup s_2^+} \frac{q(\mathbf{y}) \mathbf{r}(\mathbf{x}^+,\mathbf{y}) \cdot \mathbf{n}(\mathbf{x}^+)}{2\pi r^2(\mathbf{x}^+,\mathbf{y})}\, \mathrm{d}s(\mathbf{y}), \quad \mathbf{x}^+ \in s_1^+. \tag{9}$$

where the symbol $\oint\!\!\!\!\!\!=$ denotes the finite part of the integral in the sense of Mukherjee [34].

Eq. (9) is regularized as follows. One writes

$$\begin{aligned}\sigma(\mathbf{x}^+) = & \int_{s_1^+ - \hat{s_1}^+} \frac{q(\mathbf{y}) \mathbf{r}(\mathbf{x}^+,\mathbf{y}) \cdot \mathbf{n}(\mathbf{x}^+)}{2\pi r^2(\mathbf{x}^+,\mathbf{y})}\, \mathrm{d}s(\mathbf{y}) \\ & + \int_{\hat{s_1}^+} \frac{\mathbf{r}(\mathbf{x}^+,\mathbf{y}) \cdot [q(\mathbf{y})\mathbf{n}(\mathbf{x}^+) - q(\mathbf{x})\mathbf{n}(\mathbf{y})]}{2\pi r^2(\mathbf{x}^+,\mathbf{y})}\, \mathrm{d}s(\mathbf{y}) \\ & + \frac{q(\mathbf{x})}{2\pi} \Psi(\hat{s_1}^+, \mathbf{x}^+) \\ & + \int_{s_2^+} \frac{q(\mathbf{y}) \mathbf{r}(\mathbf{x}^+,\mathbf{y}) \cdot \mathbf{n}(\mathbf{x}^+)}{2\pi r^2(\mathbf{x}^+,\mathbf{y})}\, \mathrm{d}s(\mathbf{y}), \\ & \mathbf{x}^+ \in \hat{s}_1^+ \subset s_1^+.\end{aligned} \tag{10}$$

In the above, the angle subtended by the line element $\hat{s_1}^+$ at the point $\mathbf{x}^+$ (see [35,36] and Fig. 3) is

$$\Psi(\hat{s_1}^+, \mathbf{x}^+) = \oint\!\!\!\!\!\!= \int_{\hat{s_1}^+} \frac{\mathbf{r}(\mathbf{x}^+, \mathbf{y}) \cdot \mathbf{n}(\mathbf{y})}{r^2(\mathbf{x}^+, \mathbf{y})} \, \mathrm{d}s(\mathbf{y}) = \psi_A + \psi_B. \tag{11}$$

Also, (see Fig. 3), a unit vector $\mathbf{u}$, through the point $\mathbf{x}^+$, is chosen such that it intersects $\hat{s_1}^+$. Now, ψ is the angle between the positive $\mathbf{u}$ vector and $\mathbf{r}(\mathbf{x}^+, \mathbf{y})$ with $\mathbf{y} \in \hat{s_1}^+$. This angle can be obtained from the equation:

$$\cos(\psi(\mathbf{y})) = \frac{\mathbf{r}(\mathbf{x}^+, \mathbf{y}) \cdot \mathbf{u}}{r(\mathbf{x}^+, \mathbf{y})}. \tag{12}$$

In the above, the integrals on the right-hand side of (10) are usually regular. The last integral on the right-hand side of (10), however, becomes nearly strongly singular if the gap $2g$ is small. Once q is known on both tubes, (10) can be used, *as a post-processing step*, to obtain σ^+ and σ^- on both the beams.

2.3. Equations for straight beams

First, it should be emphasized that Eqs. (6) and (10) are valid for bent as well as for straight beams. For a pair of symmetric straight beams (see Fig. 2), let ℓ be the length of $\hat{s_1}^+$ and $\mathbf{x}^+$ be located at a distance ℓ_1 from its left end. Also, let $\ell = \ell_1 + \ell_2$. Now, Eq. (6) has the form:

$$\begin{aligned}\phi(\mathbf{x}^+) = & -\int_{s_1^+ - \hat{s_1}^+} \frac{\ln r(\mathbf{x}^+, \mathbf{y}) q(\mathbf{y})}{2\pi\varepsilon} \, \mathrm{d}s(\mathbf{y}) \\ & - \int_{\hat{s_1}^+} \frac{\ln r(\mathbf{x}^+, \mathbf{y})[q(\mathbf{y}) - q(\mathbf{x})]}{2\pi\varepsilon} \, \mathrm{d}s(\mathbf{y}) \\ & - \frac{q(\mathbf{x})}{2\pi\varepsilon}[\ell_1 \ln \ell_1 + \ell_2 \ln \ell_2 - \ell] \\ & - \int_{s_2^+} \frac{\ln r(\mathbf{x}^+, \mathbf{y}) q(\mathbf{y})}{2\pi\varepsilon} \, \mathrm{d}s(\mathbf{y}) + C, \quad \mathbf{x}^+ \in \hat{s}_1^+, \end{aligned} \tag{13}$$

where all the integrals are regular as long as g is not very small.

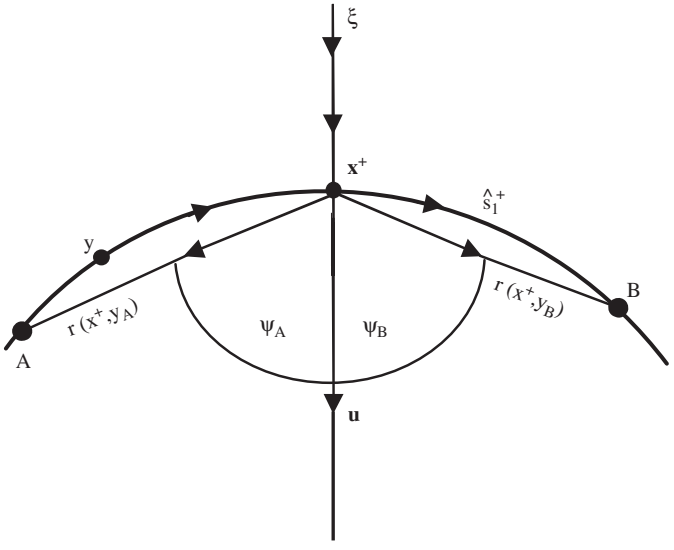

Fig. 3. Evaluation of angles.

Further, the first and second integrals on the right-hand side of (10) vanish, $\Psi = \pi$, and one is left with the simple equation:

$$\begin{aligned}&\tfrac{1}{2}[\sigma(\mathbf{x}^+) - \sigma(\mathbf{x}^-)] \\ &= \int_{s_2^+} \frac{q(\mathbf{y}) \mathbf{r}(\mathbf{x}^+, \mathbf{y}) \cdot \mathbf{n}(\mathbf{x}^+)}{2\pi r^2(\mathbf{x}^+, \mathbf{y})} \, \mathrm{d}s(\mathbf{y}), \quad \mathbf{x}^+ \in \hat{s}_1^+. \end{aligned} \tag{14}$$

Eqs. (13) and (14) are appropriate for straight nanotubes. Eq. (13) (with $q(\mathbf{y}^+) = -q(\tilde{\mathbf{y}}^+)$—see Fig. 2, $C = 0$) is used to solve for $q(\mathbf{y})$ on each beam and (14) is used, *as a post-processing step*, to calculate $\sigma(\mathbf{x}^-)$ on the upper beam.

Eq. (14) (which is a simpler version of (10)) implies that $\sigma(\mathbf{x}^+) = \sigma(\mathbf{x}^-)$ if one has only one beam. This, of course, is true. The existence of the second beam in Fig. 2 is the reason for (in general) $\sigma(\mathbf{x}^+) \neq \sigma(\mathbf{x}^-)$.

3. BIEs in semi-infinite region containing one thin conducting beam and the ground

Many problems in electrostatic simulation include a ground plane (Fig. 4(a)). The traditional approach used to solve such problems is to construct an image plane with the ground plane treated as a flat mirror (Fig. 4(b)); thereby doubling the size of the problem (Here, as shown in Eq. (19), $\phi_2 = 2\phi_G - \phi_1$). An alternative approach is to model a semi-infinite plane which includes the ground (Fig. 4(a)). The latter approach is described below.

3.1. Regular BIE

3.1.1. Source point approaching the ground surface

For a source point $\boldsymbol{\xi} \to \mathbf{x} \in \partial\hat{B}_G \subset \partial B_G$ (see Fig. 5) one has

$$\begin{aligned}\phi(\mathbf{x}) = & -\int_{\partial B_G} \frac{\sigma(\mathbf{y}) \ln r(\mathbf{x}, \mathbf{y})}{2\pi\varepsilon} \, \mathrm{d}s(\mathbf{y}) \\ & + \oint\!\!\!\!\!\!= \int_{\partial B_G} \frac{\mathbf{r}(\mathbf{x}, \mathbf{y}) \cdot \mathbf{n}(\mathbf{y}) \phi(\mathbf{y})}{2\pi r^2(\mathbf{x}, \mathbf{y})} \, \mathrm{d}s(\mathbf{y}) \\ & - \int_{s^+} \frac{q(\mathbf{y}) \ln r(\mathbf{x}, \mathbf{y})}{2\pi\varepsilon} \, \mathrm{d}s(\mathbf{y}) + C, \quad \mathbf{x} \in \partial\hat{B}_G, \end{aligned} \tag{15}$$

where $\sigma(\mathbf{y})$, $\mathbf{y} \in \partial B_G$, is the charge density, per unit length, on the ground surface.

The first integral in (15) is log singular, the second is strongly singular and the third is regular. Evaluation of the first and second integrals is discussed in Section 3.2.

3.1.2. Source point approaching the beam surface s^+

Let $\boldsymbol{\xi} \to \mathbf{x}^+ \in \hat{s}^+ \subset s^+$ (see Fig. 5). One has

$$\begin{aligned}\phi(\mathbf{x}^+) = & -\int_{\partial B_G} \frac{\sigma(\mathbf{y}) \ln r(\mathbf{x}^+, \mathbf{y})}{2\pi\varepsilon} \, \mathrm{d}s(\mathbf{y}) \\ & + \int_{\partial B_G} \frac{\mathbf{r}(\mathbf{x}^+, \mathbf{y}) \cdot \mathbf{n}(\mathbf{y}) \phi(\mathbf{y})}{2\pi r^2(\mathbf{x}^+, \mathbf{y})} \, \mathrm{d}s(\mathbf{y}) \\ & - \int_{s^+} \frac{q(\mathbf{y}) \ln r(\mathbf{x}^+, \mathbf{y})}{2\pi\varepsilon} \, \mathrm{d}s(\mathbf{y}) + C, \quad \mathbf{x}^+ \in \hat{s}^+. \end{aligned} \tag{16}$$

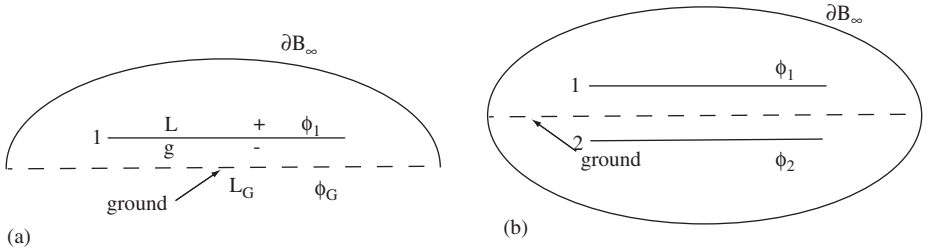

Fig. 4. Model with: (a) semi-infinite and (b) infinite plane.

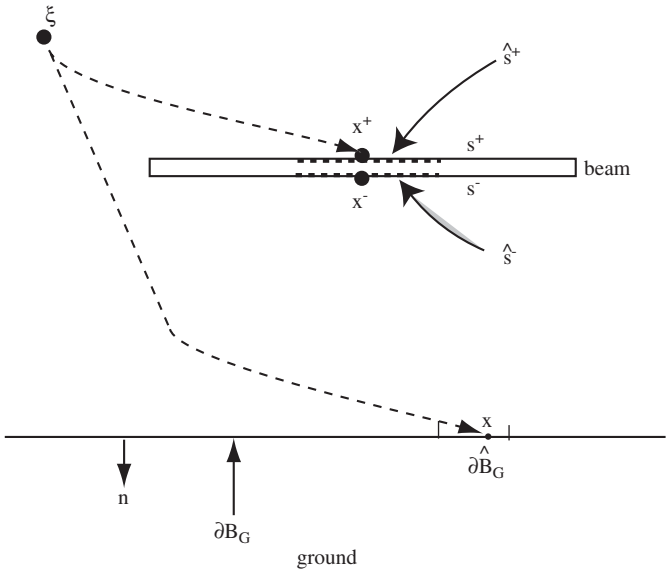

Fig. 5. Beam with ground.

This time the third integral is log singular and the rest are regular. Evaluation of the third integral in (16) is discussed in Section 3.2. With $\phi = \phi_G$, a constant, the second integral is $\phi/(2\pi)$ times the angle subtended by the ground at $\mathbf{x}^+$. Also, with the ground being straight and of infinite length, this angle equals π; so that this second integral has the value $\phi_G/2$.

3.1.3. Value of C in Eqs. (15) and (16)

Eq. (3), *for the two beam model without the ground*, is obtained from [33]

$$C = \phi_\infty \int_{\partial B_\infty} \frac{\mathbf{r}(\mathbf{x},\mathbf{y})\cdot\mathbf{n}(\mathbf{y})}{2\pi r^2(\mathbf{x},\mathbf{y})}\,\mathrm{d}s(\mathbf{y}) - \frac{\ln(R_\infty)}{2\pi\varepsilon}\,Q_\infty, \tag{17}$$

where

$$Q_\infty = \int_{\partial B_\infty} \sigma_\infty\,\mathrm{d}s(\mathbf{y}), \tag{18}$$

with σ_∞ is the charge density, per unit area, on ∂B_∞, the "surface at infinity." Assuming uniform charge distribution on ∂B_∞, one has $Q_\infty = 0 \to \sigma_\infty = 0$. Also, the integral multiplying ϕ_∞ in (17), for any source point $\mathbf{x}$ in the region of interest, is unity.

Eq. (4) is now used to evaluate the potential ϕ on the mid-line (ground) between the two beams in Fig. 4(b). With $q(\mathbf{y}^+ \in s_1^+) = -q(\tilde{\mathbf{y}}^+ \in s_2^+)$ (for corresponding points $\mathbf{y}^+$ and $\tilde{\mathbf{y}}^+$ and assuming each beam to have vanishing thickness—i.e. line models for the beams), one gets $\phi_G = C$. Next, using Appendix A of [26], one has (for $Q_\infty = 0$):

$$\phi_\infty = \phi_G = (\phi_1 + \phi_2)/2. \tag{19}$$

Finally, consider the *model with the ground* in Fig. 4(a). This time, the region of interest is semi-infinite, so that, Eq. (17) (with $\partial B\infty$ semi-infinite and $Q_\infty = 0$), yields

$$C = \phi_\infty/2 = \phi_G/2. \tag{20}$$

The expression for C from (20) can also be confirmed from Eqs. (15)–(16). First consider (15) for the special case $\phi_1 = \phi_G$. In this case the charges are zero everywhere, so that, with $\oint_{\partial B_G}[(\mathbf{r}\cdot\mathbf{n})/(2\pi r^2)]\phi(\mathbf{y})\,\mathrm{d}s(\mathbf{y}) = \phi_G/2$ (see Section 3.2.2) and $\phi(\mathbf{x}) = \phi_G$, $C = \phi_G/2$. For Eq. (16), under the same conditions, $\phi(\mathbf{x}^+) = \phi_1 = \phi_G$, $q(\mathbf{y}) = \sigma(\mathbf{y}) = 0$, $\int_{\partial B_G}[(\mathbf{r}\cdot\mathbf{n})/(2\pi r^2)]\phi(\mathbf{y})\,\mathrm{d}s(\mathbf{y}) = \phi_G/2$, so that, again, $C = \phi_G/2$.

It is also worth pointing out that, as expected, the values of the charges q and σ remain unaltered if a constant additional voltage is applied to both the beam and the ground.

Given ϕ, Eqs. (15), (16) can be solved for $\sigma(\mathbf{y})$ on ∂B_G and $q(\mathbf{y})$ on s^+.

3.2. Evaluation of singular integrals

3.2.1. First integral in (15)

This log-singular integral is evaluated as follows:

$$\begin{aligned}\int_{\partial B_G} \frac{\ln r(\mathbf{x},\mathbf{y})}{2\pi\varepsilon}\sigma(\mathbf{y})\,\mathrm{d}s(\mathbf{y}) &= \int_{\partial B_G - \partial\hat{B}_G} \frac{\ln r(\mathbf{x},\mathbf{y})}{2\pi\varepsilon}\sigma(\mathbf{y})\,\mathrm{d}s(\mathbf{y}) \\ &\quad + \int_{\partial\hat{B}_G} \frac{\ln r(\mathbf{x},\mathbf{y})}{2\pi\varepsilon}[\sigma(\mathbf{y}) - \sigma(\mathbf{x})]\,\mathrm{d}s(\mathbf{y}) \\ &\quad + \frac{\sigma(\mathbf{x})}{2\pi\varepsilon}\int_{\partial\hat{B}_G} \ln r(\mathbf{x},\mathbf{y})\,\mathrm{d}s(\mathbf{y}).\end{aligned} \tag{21}$$

A convenient way to evaluate the last log-singular integral above is given in [37].

3.2.2. Second integral in (15)

This strongly singular integral is evaluated as follows:

$$\begin{aligned}
&\oint_{\partial B_G} \frac{\mathbf{r}(\mathbf{x},\mathbf{y})\cdot\mathbf{n}(\mathbf{y})\phi(\mathbf{y})}{2\pi r^2(\mathbf{x},\mathbf{y})}\,\mathrm{d}s(\mathbf{y})\\
&\quad=\int_{\partial B_G-\partial\hat{B}_G} \frac{\mathbf{r}(\mathbf{x},\mathbf{y})\cdot\mathbf{n}(\mathbf{y})\phi(\mathbf{y})}{2\pi r^2(\mathbf{x},\mathbf{y})}\,\mathrm{d}s(\mathbf{y})\\
&\qquad+\int_{\partial\hat{B}_G} \frac{\mathbf{r}(\mathbf{x},\mathbf{y})\cdot\mathbf{n}(\mathbf{y})}{2\pi r^2(\mathbf{x},\mathbf{y})}[\phi(\mathbf{y})-\phi(\mathbf{x})]\,\mathrm{d}s(\mathbf{y})\\
&\qquad+\frac{\phi(\mathbf{x})}{2\pi}\Psi(\hat{s}^+,\mathbf{x}^+).
\end{aligned}\tag{22}$$

Please see Eq. (11) and Fig. 3 for an explanation of the angle Ψ in the last term of (22).

Since the ground line is straight, $\mathbf{r}\cdot\mathbf{n}=0$, $\Psi=\pi$, and the above integral has the value $\phi(\mathbf{x})/2$.

3.2.3. Third integral in (16)

This log-singular integral is evaluated in a manner that is analogous to Eq. (21) in Section 3.2.1.

3.3. Gradient BIE—source point approaching the beam surface s^+

The staring point here is Eqs. (8) and (16) for $\boldsymbol{\xi}\in B$. Take the gradient of (16) (at source point $\boldsymbol{\xi}$) with respect to $\boldsymbol{\xi}$, then the limit $\boldsymbol{\xi}\to\mathbf{x}^+\in s^+$, and finally take the dot product with $\mathbf{n}(\mathbf{x})$. The result is (see Fig. 5)

$$\begin{aligned}
\sigma(\mathbf{x}^+)=&\oint_{s^+}\frac{q(\mathbf{y})\mathbf{r}(\mathbf{x}^+,\mathbf{y})\cdot\mathbf{n}(\mathbf{x}^+)}{2\pi r^2(\mathbf{x}^+,\mathbf{y})}\,\mathrm{d}s(\mathbf{y})\\
&+\int_{\partial B_G}\frac{\sigma(\mathbf{y})\mathbf{r}(\mathbf{x}^+,\mathbf{y})\cdot\mathbf{n}(\mathbf{x}^+)}{2\pi r^2(\mathbf{x}^+,\mathbf{y})}\,\mathrm{d}s(\mathbf{y})\\
&-\int_{\partial B_G}\frac{\varepsilon\phi(\mathbf{y})\mathbf{n}(\mathbf{x}^+)\cdot\mathbf{n}(\mathbf{y})}{2\pi r^2(\mathbf{x}^+,\mathbf{y})}\,\mathrm{d}s(\mathbf{y})\\
&+\int_{\partial B_G}\frac{\varepsilon\phi(\mathbf{y})[\mathbf{r}(\mathbf{x}^+,\mathbf{y})\cdot\mathbf{n}(\mathbf{x}^+)][\mathbf{r}(\mathbf{x}^+,\mathbf{y})\cdot\mathbf{n}(\mathbf{y})]}{\pi r^4(\mathbf{x}^+,\mathbf{y})}\,\mathrm{d}s(\mathbf{y}).
\end{aligned}\tag{23}$$

The first term in (23) is strongly singular. It is regularized as shown in Eqs. (10)–(12).

With prescribed ϕ on ∂B_G and known $\sigma(\mathbf{y})$ on ∂B_G and $q(\mathbf{y})$ on s^+, Eq. (23) is used, as a *post-processing step*, to calculate $\sigma(\mathbf{x}^+)$ on the beam surface s^+.

A major simplification occurs when the beam is straight, the potential ϕ on the ground is constant, and the ground is straight and of infinite length. In this case, analytical integration reveals that the last two terms on the right-hand side of (23) cancel each other out! One is now left with (see Eq. (11))

$$\sigma(\mathbf{x}^+)=\frac{q(\mathbf{x})}{2}+\int_{\partial B_G}\frac{\sigma(\mathbf{y})\mathbf{r}(\mathbf{x}^+,\mathbf{y})\cdot\mathbf{n}(\mathbf{x}^+)}{2\pi r^2(\mathbf{x}^+,\mathbf{y})}\,\mathrm{d}s(\mathbf{y}).\tag{24}$$

As a consistency check, (24) collocated at $\mathbf{x}^-$ has the form:

$$\sigma(\mathbf{x}^-)=\frac{q(\mathbf{x})}{2}+\int_{\partial B_G}\frac{\sigma(\mathbf{y})\mathbf{r}(\mathbf{x}^-,\mathbf{y})\cdot\mathbf{n}(\mathbf{x}^-)}{2\pi r^2(\mathbf{x}^-,\mathbf{y})}\,\mathrm{d}s(\mathbf{y}).\tag{25}$$

In view of the relationships: $\mathbf{n}(\mathbf{x}^+)=-\mathbf{n}(\mathbf{x}^-)$, and, in the limit of a very thin beam, $\mathbf{r}(\mathbf{x}^+,\mathbf{y})=\mathbf{r}(\mathbf{x}^-,\mathbf{y})$; adding (24) and (25) gives $\sigma(\mathbf{x}^+)+\sigma(\mathbf{x}^-)=q(\mathbf{x})$.

4. BIEs in semi-infinite region containing N thin conducting beams and the ground

Consider the case with N conducting beams, with arbitrary lengths and orientations, and the ground with zero potential. (Fig. 6(a) shows an example with two beams). The typical approach for solving these problems is to reflect the beams about the ground, as shown in Fig. 6(b), and solve the problem in an infinite plane, with zero total charge on the beams. An easier way is to solve the problem in the semi-infinite plane directly. This is done below. This time, without loss of generality, ϕ_G is taken to be zero.

4.1. Regular BIEs

This time, the equations corresponding to (15) and (16) are

$$\begin{aligned}
0=&-\int_{\partial B_G}\frac{\sigma(\mathbf{y})\ln r(\mathbf{x},\mathbf{y})}{2\pi\varepsilon}\,\mathrm{d}s(\mathbf{y})\\
&-\sum_{k=1}^{N}\int_{s_k^+}\frac{q(\mathbf{y})\ln r(\mathbf{x},\mathbf{y})}{2\pi\varepsilon}\,\mathrm{d}s(\mathbf{y}),\quad \mathbf{x}\in\partial B_G,
\end{aligned}\tag{26}$$

$$\begin{aligned}
\phi_k=&-\int_{\partial B_G}\frac{\sigma(\mathbf{y})\ln r(\mathbf{x}^+,\mathbf{y})}{2\pi\varepsilon}\,\mathrm{d}s(\mathbf{y})\\
&-\sum_{j=1}^{N}\int_{s_j^+}\frac{q(\mathbf{y})\ln r(\mathbf{x}^+,\mathbf{y})}{2\pi\varepsilon}\,\mathrm{d}s(\mathbf{y}),\\
&\mathbf{x}^+\in\hat{s_k}^+,\ \ k=1,2,\ldots,N.
\end{aligned}\tag{27}$$

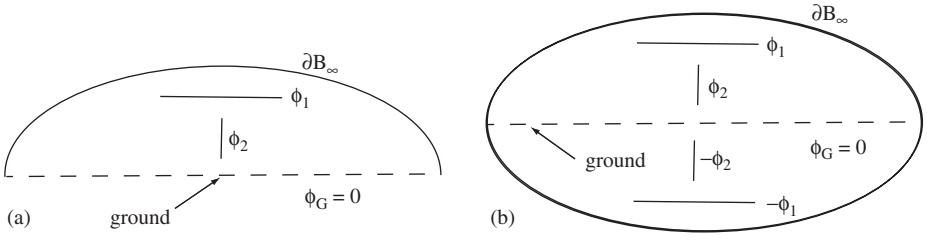

Fig. 6. Model with two beams: (a) semi-infinite and (b) infinite plane.

It is noted that (26)–(27), in which $C = 0$, satisfies $Q = 0$ where Q is the total charge on all the conductors in the infinite domain in Fig. 6(b).

Given ϕ_k, Eqs. (26), (27) can be solved for $\sigma(\mathbf{y})$ on ∂B_G and $q(\mathbf{y})$ on s_k^+.

4.2. Gradient BIE for straight beams

Eqs. (8) and (27) can be used to find the charge $\sigma(\mathbf{x}^+)$ with $\mathbf{x}^+ \in s_k^+$. One gets:

$$\sigma(\mathbf{x}^+) = \frac{q(\mathbf{x})}{2} + \int_{\partial B_G} \frac{\sigma(\mathbf{y})\mathbf{r}(\mathbf{x}^+,\mathbf{y})\cdot\mathbf{n}(\mathbf{x}^+)}{2\pi r^2(\mathbf{x}^+,\mathbf{y})}\,\mathrm{d}s(\mathbf{y}) + \sum_{\substack{j=1\\ j\neq k}}^{N} \int_{s_j^+} \frac{q(\mathbf{y})\mathbf{r}(\mathbf{x}^+,\mathbf{y})\cdot\mathbf{n}(\mathbf{x}^+)}{2\pi r^2(\mathbf{x}^+,\mathbf{y})}\,\mathrm{d}s(\mathbf{y}),$$
$$\mathbf{x}^+ \in s_k^+, \quad k = 1,2,\ldots,N, \tag{28}$$

with $q(\mathbf{x}) = \sigma(\mathbf{x}^+) + \sigma(\mathbf{x}^-)$.

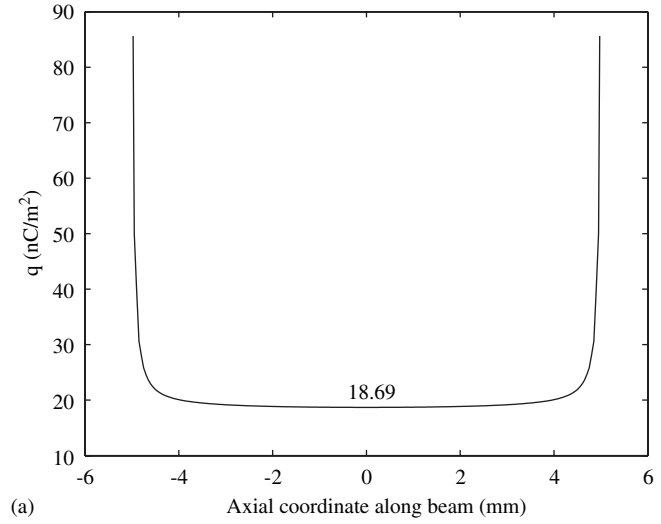

Fig. 7. Total charge density: (a) along beam and (b) along ground in a semi-infinite plane shown in Fig. 4(a). $\phi_1 = 3\,\mathrm{V}$, $\phi_G = 2\,\mathrm{V}$, $L = 10\,\mathrm{mm}$, $L_G = 100\,\mathrm{mm}$, $g/L = 0.05$, $h/L = 10^{-4}$, $\varepsilon = 8.854 \times 10^{-12}\,\mathrm{F/m}$.

5. Numerical results for beam problems with the ground

Numerical results for various problems with thin beams are presented in this section. Here, $\varepsilon = 8.854 \times 10^{-12}\,\mathrm{F/m}$. The first and last boundary elements on a beam are nonconforming ones with $\eta_1 = -0.5$, $\eta_2 = 0$, $\eta_3 = 1.0$; and $\eta_1 = -1.0$, $\eta_2 = 0$, $\eta_3 = 0.5$, respectively, to allow for singularities in q at the two ends of the beam. (Here, η, with $-1 \leqslant \eta \leqslant 1$, is the intrinsic coordinate on a quadratic boundary element and η_k, $k = 1,2,3$, are its nodal values). The rest of the elements are the usual quadratic conforming ones.

5.1. Results for a single beam with the ground

The first set of results concerns the arrangement shown in Fig. 4. This time, 100 quadratic elements are used to discretize the beam and 200 elements to discretize the ground. Again, the elements at each end of each object are nonconforming, the rest are conforming ones.

Results for the semi-infinite plane (with ground) model (Fig. 4(a)) are shown in Figs. 7 and 8. The total charge distribution along the beam and the charge distribution along the ground, from Eqs. (15), (16), appear in Figs. 7(a) and (b), respectively. Identical results are obtained for the total charge along the beam for the infinite plane arrangement shown in Fig. 4(b).

Next, the gradient Eq. (24) is used to separate the charges σ^+ and σ^- on the beam. These results are shown in Fig. 8. As expected, the charge profiles are similar to those on a thin beam [26]—almost uniform along the beam, but singular at the edges. Also, $\sigma^- \geqslant \sigma^+$ because of the proximity of the ground to the lower side of the beam in Fig. 4(a).

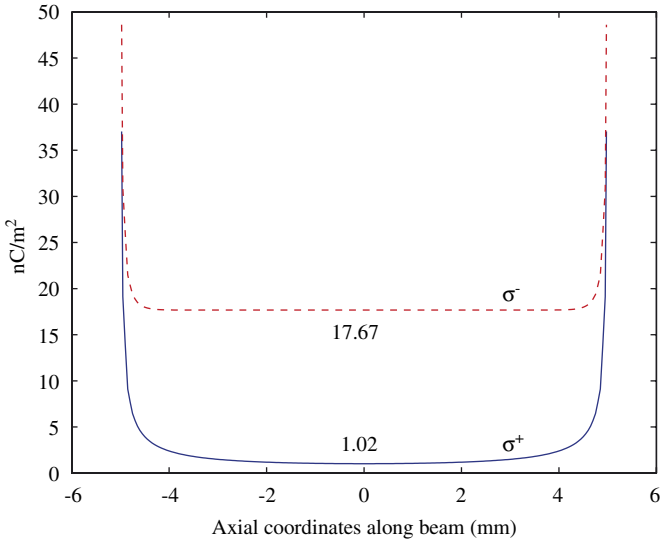

Fig. 8. Charge densities σ^+ and σ^- along beam in a semi-infinite plane shown in Fig. 4(a). $\phi_1 = 3\,\mathrm{V}$, $\phi_G = 2\,\mathrm{V}$, $L = 10\,\mathrm{mm}$, $L_G = 100\,\mathrm{mm}$, $g/L = 0.05$, $h/L = 10^{-4}$, $\varepsilon = 8.854 \times 10^{-12}\,\mathrm{F/m}$.

For a beam of infinite length with the ground, the potential gradient between the beam and the ground, for this problem, is $2\,\mathrm{V/mm} = 2000\,\mathrm{V/m}$. This number equals $\partial\phi/\partial n$ ([32, p. 152]), so that, from (8), $\sigma^- = 17.708\,\mathrm{nC/m^2}$ (assuming unit width of the beam). The numerical solution in Fig. 8, at the center of the bottom surface of the beam, is within 0.2% of this exact solution for an infinite beam.

It is also important to compare this result with previous work [26]. Fig. 8 of that paper shows the charge density at the center of the upper surface of the bottom beam (for a two beam arrangement with $\phi_1 = -1\,\mathrm{V}$, $\phi_2 = 1\,\mathrm{V}$), for $\varepsilon = 1\,\mathrm{F/m}$, to be $2000\,\mathrm{C/m^2}$. This is in agreement with the present work. (Of course, the BEM formulations employed in [26] and in the present work, for a two-beam arrangement, are identical; but the computer codes were created by different people.)

Finally, the effect of the ground length (in the computational domain), on the computed value of q at the center of the beam, is shown in Table 1. The error here refers to the percentage difference between a value of q and its value for $L_G/L = 10$ (which is the result obtained without the ground but with an image beam). It is seen that $L_G/L \geqslant 2$ gives acceptable results.

Table 1
Charge density q_0 at the center of the beam as a function of L_G/L with $L = 10\,\mathrm{mm}$, $g/L = 0.05$, $h/L = 10^{-4}$, $\varepsilon = 8.854 \times 10^{-12}\,\mathrm{F/m}$

L_G/L	q_0 (nC/m^2)	Error (%)
1	17.376	7.02
2	18.490	1.06
5	18.669	0.105
10	18.688	0

One beam with ground with $\phi_1 = 3\,\mathrm{V}$, and $\phi_G = 2\,\mathrm{V}$.

5.2. Results for two beams with the ground

The next set of results concerns the arrangement shown in Fig. 6. This time, 100 quadratic elements are used to discretize each beam and the ground. Again, the elements at each end of each object are nonconforming, the rest are conforming ones.

Results for the semi-infinite plane (with ground) model (Fig. 6(a)) are shown in Figs. 9 and 10. The total charge distributions along the beams and the charge distribution along the ground, from Eqs. (26), (27), appear in Figs. 9(a)–(c). Identical results are obtained for the total charge along each beam for the infinite plane arrangement shown in Fig. 6(b).

It is interesting to examine the results shown in Fig. 9(b). Following the heat transfer analogy, it is clear that heat would flow into beam 2 at end B, thereby leading to a negative total charge q at that end. Also, q is positive at end A. As expected, q is singular at each end, but finite results are obtained here since singular end elements are not employed in this work. The magnitude of q at end B of beam 2 is larger than that at end A. This is a consequence of the fact that $\phi_1 - \phi_2 = 2 > \phi_2 - \phi_G = 1$.

Next, the gradient Eq. (28) is used to separate the charges σ^+ and σ^- on the two beams. These results are shown in Fig. 10. As expected, the charge profiles in

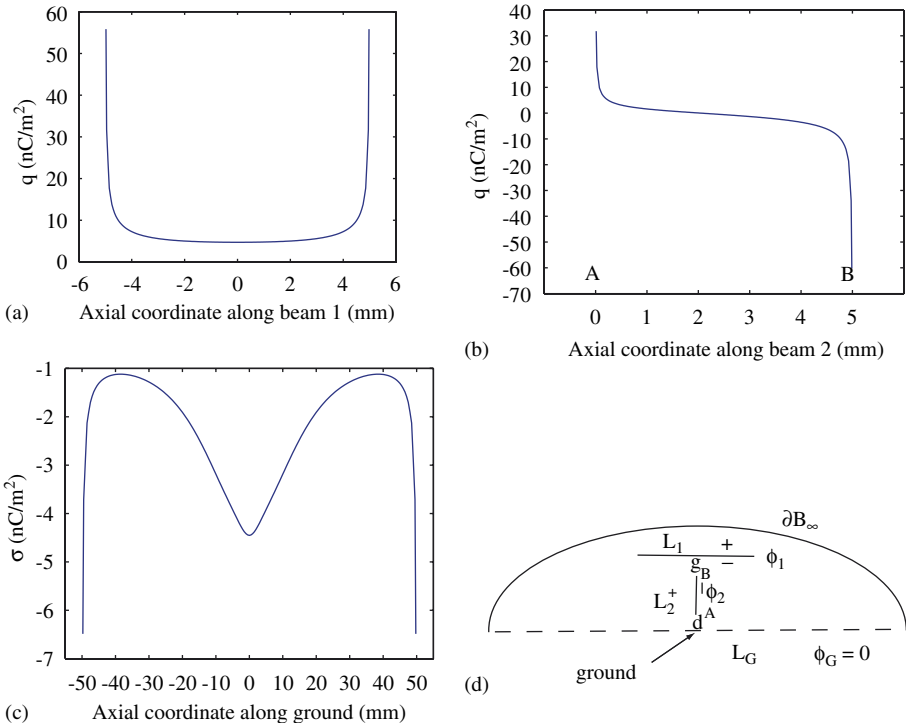

Fig. 9. Total charge density q: (a) along beam 1; (b) along beam 2 (A–B); (c) along ground; (d) a semi-infinite plane. $\phi_1 = 3$, $\phi_2 = 1$, $\phi_G = 0$, $L_1 = 10\,\mathrm{mm}$, $L_2 = 5\,\mathrm{mm}$, $L_G = 100\,\mathrm{mm}$, $g/L_1 = d/L_1 = 0.5$, $h_1/L_1 = h_2/L_2 = 10^{-4}$, $\varepsilon = 8.854 \times 10^{-12}\,\mathrm{F/m}$.

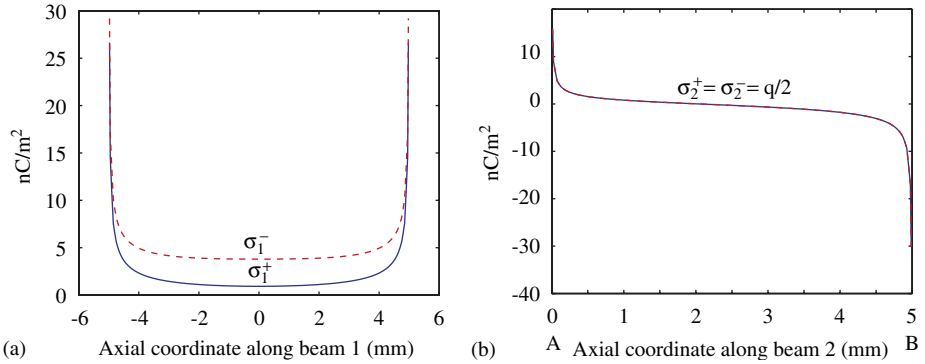

Fig. 10. Charge densities σ^+ and σ^-: (a) along beam 1; (b) along beam 2 (A–B) in a semi-infinite plane shown in Fig. 9(d). $\phi_1 = 3$, $\phi_2 = 1$, $\phi_G = 0$, $L_1 = 10\,\text{mm}$, $L_2 = 5\,\text{mm}$, $L_G = 100\,\text{mm}$, $g/L_1 = d/L_1 = 0.5$, $h_1/L_1 = h_2/L_2 = 10^{-4}$, $\varepsilon = 8.854 \times 10^{-12}\,\text{F/m}$.

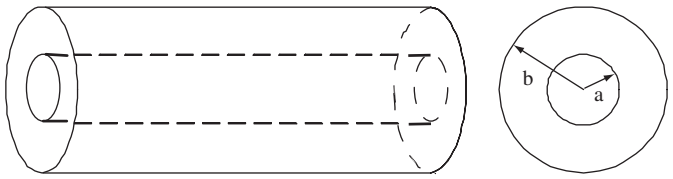

Fig. 11. A carbon nanotube.

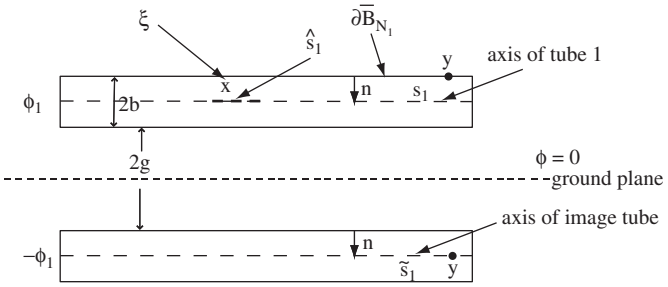

Fig. 12. Nanotube with image.

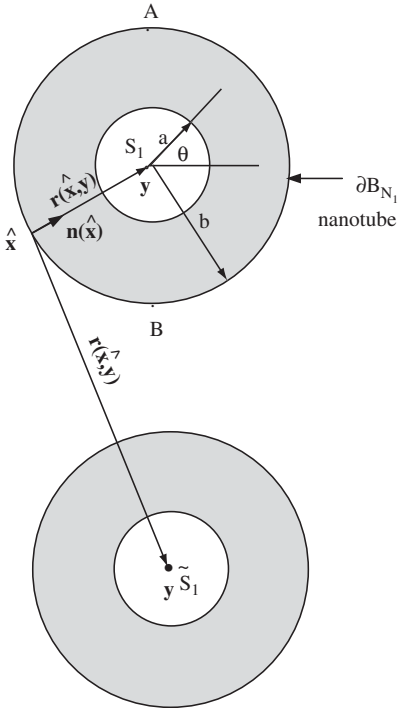

Fig. 13. Nanotube cross-section with image.

Fig. 10(a) are similar to those on a thin beam [26]—almost uniform along the beam, but singular at the edges. Also, $\sigma_1^- \geqslant \sigma_1^+$ because of the proximity of the second beam and the ground to the lower side of the first beam in Fig. 9(d). Finally, because of symmetry, $\sigma_2^+ = \sigma_2^- = q/2$ on beam 2.

6. BIEs in semi-infinite region containing one thin conducting nanotube and the ground

6.1. Nanotube models

A CNT is a thin hollow tube, of circular cross-section, as shown in Fig. 11. This figure shows a straight tube, but a CNT can be bent.

6.2. BIEs for a CNT with the ground modeled with an image tube

This section presents BIEs for a single thin conducting nanotube with an infinite ground plane (see [30]). The ground is modeled by adding on a suitable image nanotube in the computational domain (see Figs. 12 and 13).

6.2.1. Regular BIE—source point approaching the nanotube axis s_1

For a source point $\boldsymbol{\xi} \in B \to \mathbf{x} \in \hat{s}_1 \subset s_1$ (see Figs. 12 and 13), one has

$$\phi(\mathbf{x}) = \int_{\partial \bar{B}_{N_1}} \frac{q(\mathbf{y})}{4\pi\varepsilon r(\mathbf{x},\mathbf{y})}\,\mathrm{d}\ell(\mathbf{y}) + \int_{\tilde{s}_1} \frac{q(\mathbf{y})}{4\pi\varepsilon r(\mathbf{x},\mathbf{y})}\,\mathrm{d}\ell(\mathbf{y}) + C, \quad \mathbf{x} \in \hat{s}_1 \subset s_1, \tag{29}$$

with

$$q(\mathbf{y}) = \int_0^{2\pi} \sigma(y_3, b, \theta) b\,\mathrm{d}\theta, \quad y_3 \in s_1 \text{ or } \tilde{s}_1. \tag{30}$$

Here, σ is the charge density, per unit surface area, on the nanotube and q is the charge density, per unit length, on the nanotube axis s_1. The axial coordinate for a straight nanotube is y_3. For a bent nanotube, y_3 must be replaced by the arc length coordinate ℓ along the (bent) axis of the tube and the integration in (30) must be carried out on a planar cross-section of the tube that is normal to the local arc length direction.

The starting point for the first integral on the right-hand side of (29) is the double integral:

$$\int_{\partial\bar{B}_{N_1}} \mathrm{d}\ell(\mathbf{y}) \int_0^{2\pi} \frac{\sigma(\mathbf{y}) b \,\mathrm{d}\theta}{4\pi\varepsilon r(\mathbf{x},\mathbf{y})}, \tag{31}$$

where $\partial\bar{B}_{N_1}$ is a line on the nanotube surface ∂B_{N_1} which is parallel to the nanotube axis s_1. In view of (31), and the fact that $r(\mathbf{x},\mathbf{y})$ in this case is, in fact, independent of $\mathbf{y}$ (and therefore of θ), the first term on the right-hand side of (29) is exact. The second integral on the right-hand side of (29) follows from the assumption that $g \gg b$ (where g is the gap between the nanotube and the ground and b in the nanotube radius (see Figs. 12 and 13)). Therefore, one has $r(\mathbf{x},\mathbf{y}) \gg b$ and it is assumed that r is independent of θ with the field point $\mathbf{y}$ moving on the boundary of a cross-section of the image nanotube. Next, $r(\mathbf{x},\mathbf{y})$ is approximated to be the distance from $\mathbf{x} \in s_1$ and $\mathbf{y} \in \tilde{s}_1$. Exactly how large g has to be compared to b is a matter that needs further investigation. This matter is discussed in [30].

The first integral in (29) is nearly strongly singular and the second is regular. An evaluation procedure for the first integral is discussed in Section 6.4.2.

It is noted that in Fig. 12, with the charge $q(\mathbf{y})$ at a point $\mathbf{y} \in s_1$, the charge is $-q(\mathbf{y})$ at a corresponding point on the axis of the image nanotube $\mathbf{y} \in \tilde{s}_1$. Also (see the last paragraph in Section 2.1):

$$\phi_\infty = C = 0. \tag{32}$$

Therefore, $C = 0$ in (29).

Given ϕ, Eq. (29) can be solved for $q(\mathbf{y})$ on s_1.

6.2.2. Gradient BIE—source point approaching the nanotube surface ∂B_{N_1}

Let $\boldsymbol{\xi} \to \hat{\mathbf{x}} \in \partial B_{N_1}$ (see Fig. 13). Using (29) and (8), one can write

$$\sigma(\hat{\mathbf{x}}) = \int_{s_1 \cup \tilde{s}_1} \frac{\mathbf{r}(\hat{\mathbf{x}},\mathbf{y}) \cdot \mathbf{n}(\hat{\mathbf{x}}) q(\mathbf{y})}{4\pi r^3(\hat{\mathbf{x}},\mathbf{y})} \,\mathrm{d}\ell(\mathbf{y}), \quad \hat{\mathbf{x}} \in \partial B_{N_1}. \tag{33}$$

With $q(\mathbf{y})$ known, (33) can be used, *as a post-processing step*, to find the charge density distribution $\sigma(\mathbf{x})$ on the outer surface of the nanotube with axis s_1.

The integral on s_1 in (33) is nearly hypersingular. Its evaluation is discussed in Section 6.4.3. The integral on $\tilde{s}_1$ is regular.

6.3. BIEs for a CNT with an explicit model for the ground

6.3.1. Regular BIE—source point approaching the ground surface

For a source point $\boldsymbol{\xi} \in B \to \mathbf{x} \in \partial\hat{B}_G \subset \partial B_G$ (see Figs. 14 and 15), one has

$$\phi(\mathbf{x}) = \int_{\partial B_G} \frac{\sigma(\mathbf{y})}{4\pi\varepsilon r(\mathbf{x},\mathbf{y})} \,\mathrm{d}s(\mathbf{y}) + \int_s \frac{q(\mathbf{y})}{4\pi\varepsilon r(\mathbf{x},\mathbf{y})} \,\mathrm{d}\ell(\mathbf{y}) + \oint\!\!\!\!\!\!- \int_{\partial B_G} \frac{\mathbf{r}(\mathbf{x},\mathbf{y}) \cdot \mathbf{n}(\mathbf{y}) \phi(\mathbf{y})}{4\pi r^3(\mathbf{x},\mathbf{y})} \,\mathrm{d}s(\mathbf{y}) + C, \quad \mathbf{x} \in \partial\hat{B}_G \subset \partial B_G, \tag{34}$$

with

$$q(\mathbf{y}) = \int_0^{2\pi} \sigma(y_3, b, \theta) b \,\mathrm{d}\theta, \quad y_3 \in s. \tag{35}$$

Here, σ is the charge density, per unit surface area, on the nanotube and on the ground surface; and q is the charge density, per unit length, on the nanotube axis. The ground surface is ∂B_G and s is the nanotube axis. The ground is flat, with w_G the width of the ground in the y_2 direction and ℓ_G its length in the y_3 direction. (Of course, the ground is really of infinite extent but, in this work, w_G and ℓ_G are taken to be sufficiently large but finite.) Finally,

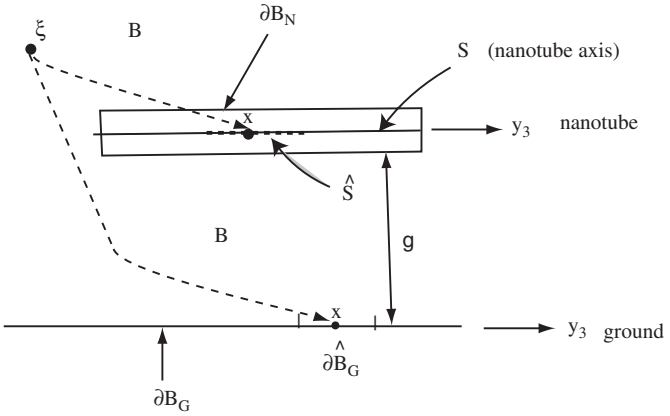

Fig. 14. Nanotube with ground.

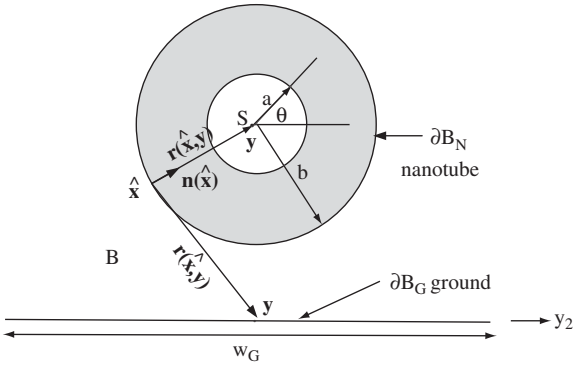

Fig. 15. Nanotube cross-section with ground.

the symbol $\neq$ in (34) denotes the finite part of the integral in the sense of Mukherjee [34].

The first and third integrals in (34) are singular and the second is regular. Evaluation procedures for the third integral is discussed in Section 6.4.1 and that of the first in Section 6.6.

6.3.2. Regular BIE—source point approaching the nanotube axis s

Let $\boldsymbol{\xi} \to \mathbf{x} \in \hat{s} \subset s$ (see Fig. 14). One has

$$\phi(\mathbf{x}) = \int_{\partial B_G} \frac{\sigma(\mathbf{y})}{4\pi\varepsilon r(\mathbf{x},\mathbf{y})}\,\mathrm{d}s(\mathbf{y}) + \int_{\partial \bar{B}_N} \frac{q(\mathbf{y})}{4\pi\varepsilon r(\mathbf{x},\mathbf{y})}\,\mathrm{d}\ell(\mathbf{y}) + \int_{\partial B_G} \frac{\mathbf{r}(\mathbf{x},\mathbf{y})\cdot\mathbf{n}(\mathbf{y})\phi(\mathbf{y})}{4\pi r^3(\mathbf{x},\mathbf{y})}\,\mathrm{d}s(\mathbf{y}) + C, \quad \mathbf{x} \in \hat{s} \subset s. \tag{36}$$

This time the first and third integrals are regular and the second is nearly strongly singular. Evaluation of the second integral in (36) is discussed in Section 6.4.2.

It is now assumed, for the rest of this paper, that $\phi(\mathbf{y}) = \phi_G$, a constant, for $\mathbf{y} \in \partial B_G$.

Also, (20) still applies, i.e.:

$$C = \phi_G/2 = \phi_\infty/2. \tag{37}$$

Given ϕ and ϕ_G, Eqs. (34), (36) can be solved for $\sigma(\mathbf{y})$ on ∂B_G and $q(\mathbf{y})$ on s.

6.3.3. Gradient BIE—source point approaching the nanotube surface ∂B_N

Let $\boldsymbol{\xi} \to \hat{\mathbf{x}} \in \partial B_N$ (see Fig. 13). Using (36) and (8), one can write

$$\sigma(\hat{\mathbf{x}}) = \int_s \frac{\mathbf{r}(\hat{\mathbf{x}},\mathbf{y})\cdot\mathbf{n}(\hat{\mathbf{x}})q(\mathbf{y})}{4\pi r^3(\hat{\mathbf{x}},\mathbf{y})}\,\mathrm{d}\ell(\mathbf{y}) + \int_{\partial B_G} \frac{\mathbf{r}(\hat{\mathbf{x}},\mathbf{y})\cdot\mathbf{n}(\hat{\mathbf{x}})\sigma(\mathbf{y})}{4\pi r^3(\hat{\mathbf{x}},\mathbf{y})}\,\mathrm{d}s(\mathbf{y}) - \int_{\partial B_G} \frac{\varepsilon\phi(\mathbf{y})\mathbf{n}(\hat{\mathbf{x}})\cdot\mathbf{n}(\mathbf{y})}{4\pi r^3(\hat{\mathbf{x}},\mathbf{y})}\,\mathrm{d}s(\mathbf{y}) + \int_{\partial B_G} \frac{3\varepsilon\phi(\mathbf{y})[\mathbf{r}(\hat{\mathbf{x}},\mathbf{y})\cdot\mathbf{n}(\hat{\mathbf{x}})][\mathbf{r}(\hat{\mathbf{x}},\mathbf{y})\cdot\mathbf{n}(\mathbf{y})]}{4\pi r^5(\hat{\mathbf{x}},\mathbf{y})}\,\mathrm{d}s(\mathbf{y}), \quad \hat{\mathbf{x}} \in \partial B_N. \tag{38}$$

With $q(\mathbf{y})$ and $\sigma(\mathbf{y})$ known, (38) can be used, *as a post-processing step*, to find the charge density distribution $\sigma(\mathbf{x})$ on the outer surface of the nanotube.

The first integral in (38) is nearly hypersingular. Its evaluation is discussed in Section 6.4.3. The last two integrals are discussed in Section 6.5.2.

6.4. Evaluation of singular integrals

6.4.1. Third integral in (34)

As mentioned before, the ground is assumed to be flat. This strongly singular integral is evaluated as follows (see [25]):

$$\neq\!\!\int_{\partial B_G} \frac{\mathbf{r}(\mathbf{x},\mathbf{y})\cdot\mathbf{n}(\mathbf{y})\phi(\mathbf{y})}{4\pi r^3(\mathbf{x},\mathbf{y})}\,\mathrm{d}s(\mathbf{y}) = \int_{\partial B_G} \frac{\mathbf{r}(\mathbf{x},\mathbf{y})\cdot\mathbf{n}(\mathbf{y})[\phi(\mathbf{y})-\phi(\mathbf{x})]}{4\pi r^3(\mathbf{x},\mathbf{y})}\,\mathrm{d}s(\mathbf{y}) + \frac{\phi(\mathbf{x})}{4\pi}\neq\!\!\int_{\partial B_G} \frac{\mathbf{r}(\mathbf{x},\mathbf{y})\cdot\mathbf{n}(\mathbf{y})}{r^3(\mathbf{x},\mathbf{y})}\,\mathrm{d}s(\mathbf{y}). \tag{39}$$

The solid angle subtended by the flat surface ∂B_G at $\mathbf{x} \in \partial B_G$ (in the sense of an FP integral with $\boldsymbol{\xi} \in B \to \mathbf{x} \in \partial B_G$) is

$$\Omega(\partial B_G, \mathbf{x}) = \neq\!\!\int_{\partial B_G} \frac{\mathbf{r}(\mathbf{x},\mathbf{y})\cdot\mathbf{n}(\mathbf{y})}{r^3(\mathbf{x},\mathbf{y})}\,\mathrm{d}s(\mathbf{y}) = 2\pi. \tag{40}$$

The first integral on the right-hand side of (39), which is weakly singular, vanishes on a flat ground since $\mathbf{r}\cdot\mathbf{n} = 0$. With $\phi(\mathbf{x}) = \phi_G$ for $\mathbf{x} \in \partial B_G$, one finally gets

$$\neq\!\!\int_{\partial B_G} \frac{\mathbf{r}(\mathbf{x},\mathbf{y})\cdot\mathbf{n}(\mathbf{y})\phi(\mathbf{y})}{4\pi r^3(\mathbf{x},\mathbf{y})}\,\mathrm{d}s(\mathbf{y}) = \frac{\phi_G}{2}. \tag{41}$$

6.4.2. Second integral in (36) (same as first integral in (29))

This nearly strongly singular integral is evaluated as follows (see Fig. 16):

$$\int_{\partial \bar{B}_N} \frac{q(\mathbf{y})}{4\pi\varepsilon r(\mathbf{x},\mathbf{y})}\,\mathrm{d}\ell(\mathbf{y}) = \int_{\partial \bar{B}_N - \partial \hat{\bar{B}}_N} \frac{q(\mathbf{y})}{4\pi\varepsilon r(\mathbf{x},\mathbf{y})}\,\mathrm{d}\ell(\mathbf{y}) + \int_{\partial \hat{\bar{B}}_N} \frac{z}{r(\mathbf{x},\mathbf{y})}\frac{[q(\mathbf{y})-q(\hat{\mathbf{x}})]}{4\pi\varepsilon z}\,\mathrm{d}\ell(\mathbf{y}) + \frac{q(\hat{\mathbf{x}})}{4\pi\varepsilon}\int_{-\hat{\ell}/2}^{\hat{\ell}/2} \frac{\mathrm{d}z}{\sqrt{z^2+b^2}}, \quad \mathbf{x} \in \text{ center of } \hat{s}, \tag{42}$$

where the length of the nanotube segment $\hat{s}$ is $\hat{\ell}$. This segment is assumed to be straight and the last integral on the right-hand side of (42), which is nearly strongly singular, is evaluated analytically.

Please note that the field point $\mathbf{y}$ is placed on the outer surface ∂B_N of the nanotube while the source point $\mathbf{x}$ lies on its axis s. The quantity $z/r(\mathbf{x},\mathbf{y})$ in the second integral on the right-hand side of (42) is $\mathcal{O}(1)$ and $\to 0$ as $\mathbf{y} \to \hat{\mathbf{x}}$. Therefore, the total integrand in this integral is regular.

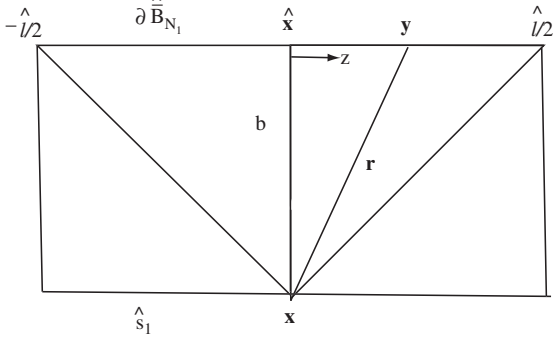

Fig. 16. Evaluation of last integral in (42).

(See [25] for the use of a similar idea for the evaluation of nearly weakly singular integrals.)

Finally, it is assumed that $q(\mathbf{x}) = q(\hat{\mathbf{x}})$ in (42). The source point $\mathbf{x}$ is at the mid-point of $\hat{s}$ in the last integral on the right-hand side of (42) (see Fig. 16). Please refer to the Appendix of [30] for the general situation where $\mathbf{x}$ is any point on $\hat{s}$.

6.4.3. First integral in (38) (same as integral on s_1 in (33))

This nearly hypersingular integral is evaluated as follows:

$$\begin{aligned}
&\int_s \frac{\mathbf{r}(\hat{x},\mathbf{y})\cdot\mathbf{n}(\hat{\mathbf{x}})q(\mathbf{y})}{4\pi r^3(\hat{\mathbf{x}},\mathbf{y})}\,\mathrm{d}\ell(\mathbf{y})\\
&\quad=\int_{s-\hat{s}} \frac{\mathbf{r}(\hat{\mathbf{x}},\mathbf{y})\cdot\mathbf{n}(\hat{\mathbf{x}})q(\mathbf{y})}{4\pi r^3(\hat{\mathbf{x}},\mathbf{y})}\,\mathrm{d}\ell(\mathbf{y})\\
&\qquad+\int_{\hat{s}} \frac{\mathbf{r}(\hat{\mathbf{x}},\mathbf{y})\cdot\mathbf{n}(\hat{\mathbf{x}})[q(\mathbf{y})-q(\bar{\mathbf{x}})-q'(\bar{\mathbf{x}})(\mathbf{y}-\bar{\mathbf{x}})]}{4\pi r^3(\hat{\mathbf{x}},\mathbf{y})}\,\mathrm{d}\ell(\mathbf{y})\\
&\qquad+q(\bar{\mathbf{x}})\int_{\hat{s}} \frac{\mathbf{r}(\hat{\mathbf{x}},\mathbf{y})\cdot\mathbf{n}(\hat{\mathbf{x}})}{4\pi r^3(\hat{\mathbf{x}},\mathbf{y})}\,\mathrm{d}\ell(\mathbf{y})\\
&\qquad+q'(\bar{\mathbf{x}})\int_{\hat{s}} \frac{\mathbf{r}(\hat{\mathbf{x}},\mathbf{y})\cdot\mathbf{n}(\hat{\mathbf{x}})(\mathbf{y}-\bar{\mathbf{x}})}{4\pi r^3(\hat{\mathbf{x}},\mathbf{y})}\,\mathrm{d}\ell(\mathbf{y}),\\
&\quad\hat{\mathbf{x}}\in\partial\hat{B}_N\subset\partial B_N,
\end{aligned}\tag{43}$$

where $\bar{\mathbf{x}}\in\hat{s}$ is closest to $\hat{\mathbf{x}}\in\partial B_N$ (see Fig. 17). Also, $\hat{\mathbf{x}}$ is at the mid-point of the segment $\partial\hat{B}_N$ of ∂B_N. This is sufficient since (33) is a post-processing step.

Referring to Fig. 17, for a piecewise quadratic approximation for $q(\mathbf{y})$, the second integral on the right-hand side of (43) (using the Taylor series for $q(\mathbf{y})$ about $\bar{\mathbf{x}}$) becomes:

$$\frac{q''(\bar{\mathbf{x}})}{8\pi}\int_{-\hat{\ell}/2}^{\hat{\ell}/2}\frac{bz^2\,\mathrm{d}z}{(z^2+b^2)^{3/2}}.\tag{44}$$

This integral can be evaluated analytically.

Again referring to Fig. 17, the third integral on the right-hand side of (43) becomes:

$$q(\bar{\mathbf{x}})\int_{\hat{s}}\frac{\mathbf{r}(\hat{\mathbf{x}},\mathbf{y})\cdot\mathbf{n}(\hat{\mathbf{x}})}{4\pi r^3(\hat{\mathbf{x}},\mathbf{y})}\,\mathrm{d}\ell(\mathbf{y})=\frac{q(\bar{\mathbf{x}})}{4\pi}\int_{-\hat{\ell}/2}^{\hat{\ell}/2}\frac{b\,\mathrm{d}z}{(z^2+b^2)^{3/2}}.\tag{45}$$

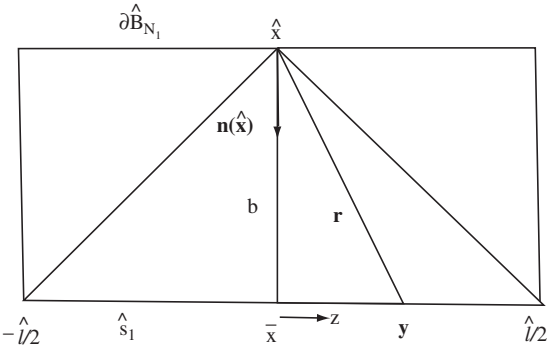

Fig. 17. Evaluation of third integral in (43).

This integral can be evaluated analytically. The last integral on the right-hand side of (43) is

$$\begin{aligned}
&q'(\bar{\mathbf{x}})\int_{\hat{s}}\frac{\mathbf{r}(\hat{\mathbf{x}},\mathbf{y})\cdot\mathbf{n}(\hat{\mathbf{x}})(\mathbf{y}-\bar{\mathbf{x}})}{4\pi r^3(\hat{\mathbf{x}},\mathbf{y})}\,\mathrm{d}\ell(\mathbf{y})\\
&\quad=\frac{q'(\bar{\mathbf{x}})}{4\pi}\int_{-\hat{\ell}/2}^{\hat{\ell}/2}\frac{bz\,\mathrm{d}z}{(z^2+b^2)^{3/2}}=0.
\end{aligned}\tag{46}$$

Finally, (43) has the simple form

$$\begin{aligned}
&\int_s\frac{\mathbf{r}(\hat{x},\mathbf{y})\cdot\mathbf{n}(\hat{\mathbf{x}})q(\mathbf{y})}{4\pi r^3(\hat{\mathbf{x}},\mathbf{y})}\,\mathrm{d}\ell(\mathbf{y})\\
&\quad=\int_{s-\hat{s}}\frac{bq(\mathbf{y})}{4\pi r^3(\hat{\mathbf{x}},\mathbf{y})}\,\mathrm{d}\ell(\mathbf{y})+\frac{q''(\bar{\mathbf{x}})}{8\pi}\int_{-\hat{\ell}/2}^{\hat{\ell}/2}\frac{bz^2\,\mathrm{d}z}{(z^2+b^2)^{3/2}}\\
&\qquad+\frac{q(\bar{\mathbf{x}})}{4\pi}\int_{-\hat{\ell}/2}^{\hat{\ell}/2}\frac{b\,\mathrm{d}z}{(z^2+b^2)^{3/2}},\quad\hat{\mathbf{x}}\in\partial\hat{B}_N\subset\partial B_N.
\end{aligned}\tag{47}$$

It is easy to observe from (33) and (47) that, for a single nanotube without the ground, $\sigma(\hat{\mathbf{x}})$, on any cross-section of a nanotube, is, as expected, axisymmetric.

6.5. Evaluation of integrals containing constant potentials

6.5.1. Third integral in (36)

It is first observed that, for any $\boldsymbol{\xi}\in B$, one has

$$\int_{\partial B_G}\frac{\mathbf{r}(\boldsymbol{\xi},\mathbf{y})\cdot\mathbf{n}(\mathbf{y})}{r^3(\boldsymbol{\xi},\mathbf{y})}\,\mathrm{d}s(\mathbf{y})=\Omega(\partial B_G,\boldsymbol{\xi}),\tag{48}$$

where $\Omega(\partial B_G,\boldsymbol{\xi})$ is the solid angle subtended by ∂B_G at $\boldsymbol{\xi}$. Since the ground ∂B_G is an infinite plane, $\Omega=2\pi$ for any point $\boldsymbol{\xi}\in B$ that is "near" the ground in the sense that the ground is very large compared to the shortest distance between $\boldsymbol{\xi}$ and the ground. Therefore, with $\boldsymbol{\xi}=\mathbf{x}$ on the nanotube axis, and $\phi(\mathbf{y})=\phi_G$, the third integral on the right-hand side of (36) equals $\phi_G/2$.

6.5.2. Third and fourth integrals in (38)

These two integrals together arise from the gradient ∇_ξ of the integral on the left-hand side of (48) with its integrand multiplied by $\phi(\mathbf{y})/(4\pi)$. As stated above, when $\phi(\mathbf{y})=\phi_G$, a constant, and $\boldsymbol{\xi}$ is near the ground, this integral (i.e. the one in (48) multiplied by $\phi_G/(4\pi)$) is a constant (of value $\phi_G/2$); so that its gradient with respect to $\boldsymbol{\xi}$ vanishes. Therefore, the third and fourth integrals on the right-hand side of (38), together, vanish! (Please see Section 3.3 for a similar conclusion in the 2D case).

6.6. Evaluation of integrals on the ground

Consider the first integrals in (34) and (36) and the second in (38). The domains of these surface integrals is the ground ∂B_G. The first of these integrals is weakly singular and the rest are regular.

In all these cases, the 2D ground is discretized into piecewise constant rectangular elements. Analytical inte-

gration in employed for the singular element in the first integral. All other integrals are evaluated by usual Gauss quadrature.

7. Numerical results for nanotube problems with the ground

Numerical results are presented in this section for the problem of one nanotube with the ground in semi-infinite space (see Fig. 4(a) for the corresponding beam problem). Detailed results for nanotube problems with the ground modeled with image tubes are available in [30].

The nanotube is parallel to the ground and is positioned with respect to it in symmetric fashion, as shown in Fig. 18(a). 1D quadratic elements are used along the nanotube. The first and last elements on the tube are nonconforming ones (see the first paragraph of Section 5); the rest are the usual quadratic conforming ones. The 2D ground is modeled with constant rectangular elements. The number of elements on the nanotube, and along the length and width of the ground, are $N_N = 101$, $N_L = 100$, $N_W = 35$, respectively.

Results for the total charge q per unit length on the nanotube appear in Fig. 18(b) while the corresponding charge density σ per unit area on the ground appear in Fig. 19. As before, $\varepsilon = 8.854 \times 10^{-12}\,\mathrm{F/m}$.

The analytical solution for the charge distribution q, per unit length, on a conducting tube of infinite length, of radius b, parallel to, and at a distance g from the ground (the axis of the tube is at a distance $b+g$ from the ground) is [32]

$$q = \frac{2\pi\varepsilon\phi}{\cosh^{-1}(1+g/b)}, \tag{49}$$

with ϕ the potential on the tube and zero potential on the ground. For the case shown in Fig. 18(b), the analytical result is 16.0563 pC/m, while the numerical solution at the center of the nanotube is 16.0480 pC/m. The error is 0.05%.

As a further check of the results shown in Figs. 18(b) and 19, the total charge on the nanotube and the ground are obtained by numerical integration of the charge densities shown in these figures. In view of the facts that the charge density is singular at the two ends of the nanotube, and that singular end elements have not been employed, contributions from the first and last elements on the nanotube are ignored for the time being. The calculated total charge on the nanotube is 15.789 aC while that on the ground is −15.404 aC. The absolute values of these numbers agree within 2.44%.

The effect of the size of the ground plane (in the computational domain), on the value of q at the center of the nanotube, appears in Table 2. The error is calculated with respect to the exact solution for a nanotube of infinite length, which is 16.0480 pC/m. It is seen that one needs, at least, $L_G/L_N \approx 4$ and $w_G/g \approx 4$, in order to get results of acceptable accuracy.

8. Concluding remarks

This paper presents a simple way to model the ground plane in problems involving conducting beams and

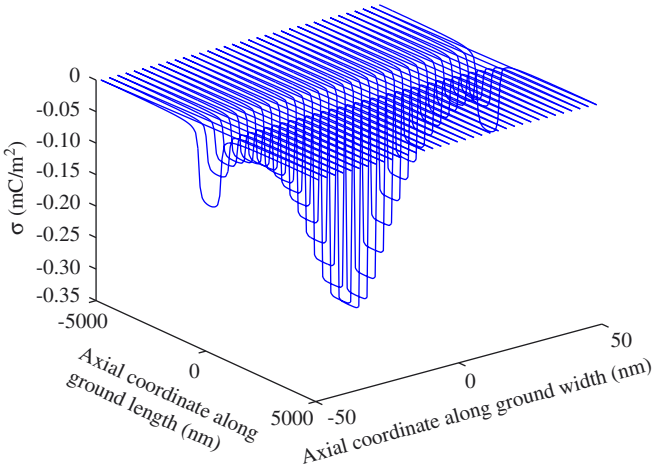

Fig. 19. Charge density σ per unit area along ground. $L_N = 1000\,\mathrm{nm}$, $b = 1\,\mathrm{nm}$, $g = 15\,\mathrm{nm}$, $L_G = 10,000\,\mathrm{nm}$, $w_G = 100\,\mathrm{nm}$, $\phi_N = 1\,\mathrm{V}$, $\phi_G = 0\,\mathrm{V}$, $\varepsilon = 8.854 \times 10^{-12}\,\mathrm{F/m}$.

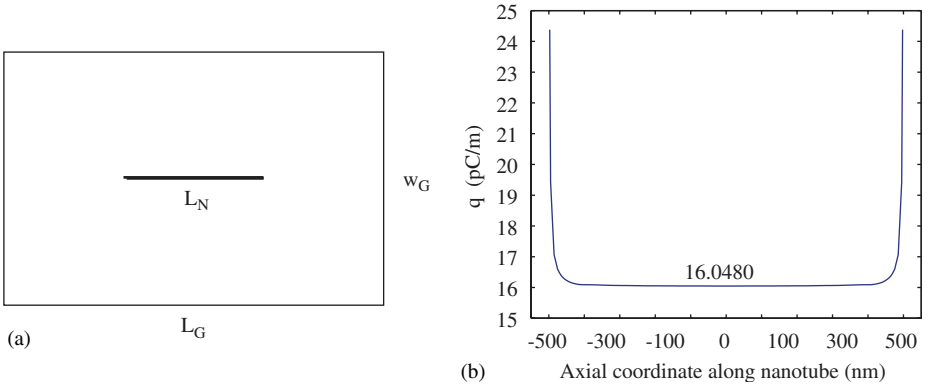

Fig. 18. (a) Top view of nanotube with ground. (b) Charge density q per unit length along nanotube. $L_N = 1000\,\mathrm{nm}$, $b = 1\,\mathrm{nm}$, $g = 15\,\mathrm{nm}$, $L_G = 10,000\,\mathrm{nm}$, $w_G = 100\,\mathrm{nm}$, $\phi_N = 1\,\mathrm{V}$, $\phi_G = 0\,\mathrm{V}$, $\varepsilon = 8.854 \times 10^{-12}\,\mathrm{F/m}$.

Table 2
Charge density q_0 at the center of the nanotube as a function of L_G and w_G with $L_N = 1000\,\text{nm}$, $b = 1\,\text{nm}$, $g = 15\,\text{nm}$, $\phi_N = 1\,\text{V}$, $\phi_G = 0\,\text{V}$, $\varepsilon = 8.854 \times 10^{-12}\,\text{F/m}$.

L_G (nm)	w_G (nm)	q_0 (pC/m)	Error (%)
1000	15	14.1623	11.8
2000	30	15.1713	5.5
4000	60	15.7916	1.65
8000	90	15.8946	0.38
10,000	100	16.0480	0.05

nanotubes for the purpose of applying the BEM to obtain charge distributions on them in electrostatic problems. The beams are modeled as lines in a semi-infinite plane; while the nanotubes are modeled as lines in a half-space. The ground plane is modeled directly—as a line for beams and as a plane for nanotubes.

The present paper only deals with conductors for which the external Dirichlet problem for Laplace's equation is applicable. Mixed boundary conditions can also be handled but would require the full BIE rather than the truncated one (2). An example is semi-conducting nanotubes that, for a Laplace/Poisson semi-classical model, require matching potentials and prescribed charge difference across the nanotube surface. An example of this situation, with the boundary cloud method (BCM) (a mesh-free version of the standard rather than the thin feature BIE), is available in [22]. Research along these lines, with a thin feature BEM, is currently in progress at Cornell.

The ground, in real life, is of infinite extent, but is finite for the computations. The chosen dimensions for the ground, for computations, must be large enough in order to get accurate results. Based on the results in Tables 1 and 2, the following recommendations are made:

- for 2D beam problems: $L_G/L \geqslant 2$;
- for 3D nanotube problems: $L_G/L_N \geqslant 4$, $w_G/g \geqslant 4$.

Acknowledgments

This research has been supported by Grant # CMS-0508466 of the National Science Foundation to Cornell University. Sincere thanks are expressed to David Roundy and Arend Vanderzande, of the Physics department at Cornell, for their many useful suggestions during the course of this research.

References

[1] Roukes ML. Nanoelectromechanical Systems. Solid-state sensor and actuator workshop. Hilton Head, SC; 2000.
[2] Davis ZJ, Abadal G, Kuhn O, Hansen O, Grey F, Boisen A. Fabrication and characterization of nanoresonating devices for mass detection. J Vacuum Sci Technol B 2000;18:612–6.
[3] Boggild P, Hansen TM, Tanasa T, Grey F. Fabrication and actuation of customized nanotweezers with a 25 nm gap. Nanotechnology 2001;12:331–5.
[4] Cleland AL, Roukes ML. Fabrication of high frequency nanometer scale mechanical resonators from bulk Si crystals. Appl Phys Lett 1996;69.
[5] Sazonova V, Yaish Y, Üstünel H, Roundy D, Arias TA, McEuen PL. A tunable carbon nanotube electromechanical oscillator. Nature 2004;431:284–7.
[6] Mukherjee S. Boundary element methods in creep and fracture. London: Applied Science Publishers; 1982.
[7] Banerjee PK. The boundary element methods in engineering. Maidenhead, Berkshire, England: McGraw Hill Europe; 1994.
[8] Chandra A, Mukherjee S. Boundary element methods in manufacturing. New York: Oxford University Press; 1997.
[9] Bonnet M. Boundary integral equation methods for solids and fluids. Chichester, UK: Wiley; 1999.
[10] Mukherjee S, Mukherjee YX. Boundary methods: elements contours and nodes. Boca Raton, FL: Taylor and Francis, CRC Press; 2005.
[11] Yang TY. Finite element structural analysis. Englewood Cliffs, NJ: Prentice-Hall; 1986.
[12] Zienkiewicz OC, Taylor RL. The finite element method, vols. 1,2, 4th ed. Maidenhead, Berkshire, UK: McGraw-Hill; 1994.
[13] Hughes TJR. The finite element method: linear static and dynamic finite element analysis. Mineola, NY: Dover; 2000.
[14] Senturia SD, Harris RM, Johnson BP, Kim S, Nabors K, Shulman MA, White JK. A computer-aided design system for microelectromechanical systems (MEMCAD). J Micro-Electro-Mechanical Syst 1992;1:3–13.
[15] Nabors K, White J. FastCap: a multi-pole accelerated 3-D capacitance extraction program. IEEE Trans Comput Aided Design Integrated Circuits Syst 1991;10:1447–59.
[16] Gilbert JR, Legtenberg R, Senturia SD. 3D coupled electromechanics for MEMS: applications of CoSolve-EM. Proceedings IEEE MEMS 1995, pp. 122–7.
[17] Shi F, Ramesh P, Mukherjee S. Simulation methods for micro-electro-mechanical structures (MEMS) with application to a microtweezer. Comput Struct 1995;56:769–83.
[18] Aluru NR, White J. An efficient numerical technique for electromechanical simulation of complicated microelectromechanical structures. Sensors Actuators A 1997;58:1–11.
[19] Mukherjee S, Bao Z, Roman M, Aubry N. Nonlinear mechanics of MEMS plates with a total Lagrangian approach. Comput Struct 2005;83:758–68.
[20] Shi F, Ramesh P, Mukherjee S. Dynamic analysis of micro-electro-mechanical systems. Int J Numer Meth Eng 1996;39:4119–39.
[21] De SK, Aluru NR. Full-Lagrangian schemes for dynamic analysis of electrostatic MEMS. J Microelectromechanical Syst 2004;13:737–58.
[22] Tang Z, Xu Y, Li G, Aluru NR. Physical models for coupled electromechanical analysis of silicon nanoelectromechanical systems. J Appl Phys 2005;97(1–13):114304.
[23] Frangi A, di Gioia A. Multipole BEM for the evaluation of damping forces on MEMS. Comput Mech 2005;37:24–31.
[24] Harrington RF. Field computation by moment methods. Piscataway, NJ: IEEE Press; 1993.
[25] Bao Z, Mukherjee S. Electrostatic BEM for MEMS with thin conducting plates and shells. Eng Anal Boundary Elements 2004;28:1427–35.
[26] Bao Z, Mukherjee S. Electrostatic BEM for MEMS with thin beams. Commun Numer Meth Eng 2005;21:297–312.
[27] Chuyan SW, Liao YS, Chen JT. Computational study of the effect of finger width and aspect ratios for the electrostatic levitating force of MEMS combdrive. J Microelectromechanical Syst 2005;14:305–12.

[28] Telukunta S, Mukherjee S. Fully Lagrangian modeling of MEMS with thin plates, J Microelectromechanical Syst 2006;15: 795–810.
[29] Mukherjee S, Telukunta S, Mukherjee YX. BEM modeling of damping forces on MEMS with thin plates. Eng Anal Boundary Elements 2005;29:1000–7.
[30] Chen H, Mukherjee S. Charge distribution on thin conducting nanotubes—reduced 3-D model, Int J Numer Meth Eng 2006, in press.
[31] Ke C, Espinosa HD. Numerical analysis of nanotube-based NEMS devices—part I: Electrostatic charge distribution on multiwalled nanotubes. ASME J Appl Mech 2005;72:721–5.
[32] Hayt W, Buck J. Engineering a electromagnetics, 6th ed. New York: McGraw-Hill; 2001.
[33] Shi F, Ramesh P, Mukherjee S. On the application of 2D potential theory to electrostatic simulation. Commun Numer Meth Eng 1995;11:691–701.
[34] Mukherjee S. Finite parts of singular and hypersingular integrals with irregular boundary source points. Eng Anal Boundary Elements 2000;24:767–76.
[35] Phan A-V, Mukherjee S, Mayer JRR. A boundary contour method for two-dimensional linear elasticity with quadratic boundary elements. Comput Mech 1997;20:310–9.
[36] Mukherjee S. CPV and HFP integrals and their applications in the boundary element method. Int J Solids Struct 2000;37:6623–34.
[37] Telukunta S, Mukherjee S. An extended boundary node method for modeling normal derivative discontinuities in potential theory across edges and corners. Eng Anal Boundary Elements 2004;28:1099–110.